Aerospace Science and Technology 28 (2013) 164–175

Contents lists available at SciVerse ScienceDirect

Aerospace Science and Technology

www.elsevier.com/locate/aescte

Investigation of drag and wake turbulence of a rotor hub ☆

Vrishank Raghav *,[1], Rajiv Shenoy *,[1], Marilyn Smith **,[2], Narayanan Komerath **,[2]

Daniel Guggenheim School of Aerospace Engineering, Georgia Institute of Technology, Atlanta, GA 30332-0150, USA

ARTICLE INFO

Article history:
Received 26 June 2012
Received in revised form 24 October 2012
Accepted 30 October 2012
Available online 10 November 2012

Keywords:
Hub drag
Hub wake
PIV
CFD
Rotating hub
Helicopter
Rotorcraft
Complex configuration

ABSTRACT

Hubs of rotating systems have a significant contribution to the total vehicle parasite drag. The complexity of hub configurations and of the flows around them leads to large uncertainty in drag prediction at the design stage, which inhibits the development of advanced concepts. A generic, modular hub configuration is used in a wind tunnel to deconstruct and resolve drag contributions, and to reduce the uncertainty in prediction and measurement. Predictions are made with the same configuration, including tunnel walls and support structure in flow field computations, using an overset, unstructured Navier–Stokes approach with mesh adaptation. A progression of results is presented; surface pressure calculations are used to compute integrated drag on the non-rotating and rotating configurations at various levels of assembly. These calculations are also used to extract interaction effects and causal physics. Experimental and computational wake velocity fields are compared for velocity deficits and shear layers. Measured and computed velocity profiles and turbulence spectra measurements in the hub near wake (0.5–1.0 hub diameters) correlate well when proper fidelity of grid, time step, and turbulence model are chosen. The wake spectral content is characterized by broadband turbulence in addition to large scale spectral content energizing the flow field.

1. Introduction

Recent helicopter design has focused on achieving higher forward flight speeds. A major obstacle the designers have had to overcome is the limitation of parasite drag on forward flight performance [14,31]. Clearly a reduction in parasite drag will increase the vehicle's range, maximum speed and payload. In addition, it has been shown to improve the vehicle stability and control [11] and decrease the vibrational excitation and blade loads [13], resulting in weight reduction and blade life extension. The main contributors of parasite drag on a helicopter include the fuselage, main rotor pylon and hub, all protuberances such as landing gear and antennae, and engine protrusions. The hub of single main rotor helicopters has been found to contribute approximately 25–30% of the vehicle parasite drag [9], while coaxial hubs yield as much as 50%, as is the case with the XH-59 [30]. This factors to be around 10% of the total power required by the helicopter. To facilitate better hub designs with considerable reductions in drag, the sources of drag and physics behind the phenomena must be better understood, modeled and predicted. The lack of fundamental knowledge for such non-aerodynamic forms which encompass the hub assembly requires further investigation.

Major challenges in measuring and predicting hub drag are the following:

1. Complex geometry
   (a) The complex geometry leading to flow interactions over the hub creating interference drag which is hard to interpret.
   (b) Interactions augmented by presence of fine structures such as tubes, wires, linkages and fasteners.
2. Effect of rotation
   (a) Consideration of all hub structures in a typical assembly requires the analysis of a large range of Reynolds number effects.
   (b) Measurement and prediction of drag of rotating components are a challenge in itself.
   (c) In particular, for high speed applications, the hub may experience compressibility effects, adding a new dimension of complexity.

Prior experimental research of hub drag is mostly directed toward improving drag characteristics of current hub designs by the addition of fairings. Fairing designs have been explored by industry [30] to reduce flow separation and interference drag between the hub and fuselage. To date, frontal swept area of the hub design has been the leading parameter tied to hub drag [27], therefore the fairing of an existing hub design does not address the issue

☆ Most figures in this article are in color only in the electronic version.

* Corresponding authors.
** Principal corresponding authors.
E-mail address: komerath@gatech.edu (N. Komerath).
[1] Ph.D. Candidate.
[2] Professor.

1270-9638/$ – see front matter
http://dx.doi.org/10.1016/j.ast.2012.10.012

directly. This is especially true for articulated hubs, where empty space is required for the control hinges. While empirically corrected analytic estimates have been developed to predict hub drag based on frontal area, there is no consistent trend when accounting for interference effect and frontal swept area [26]. Considerations for hub displacement from the fuselage have been made, weighing the effects of increased frontal area to decreased interference [27]. Bridgeman and Lancaster [5] have successfully computed drag to within 5% of experimental values on a 1/5 scale helicopter for various pitch attitudes.

A typical helicopter hub is comprised of a myriad of bluff-body components, mainly due to compromises in manufacturing procedures. The distinction between streamlined and bluff bodies is associated with the poor performance characteristics (such as lift to drag ratio) of the latter configurations. The primary drag component in these bluff bodies is due to flow separation rather than viscous effects. The pressure drag of bluff bodies results from vortices in the wake that are shed from the structure.

Bluff-body wakes associated with rotor hub components affect the performance of both commercial and military air vehicles [10]. While many studies of two-dimensional (2D) bluff bodies have been performed in the past, three-dimensional (3D) studies have been typically restricted to spheres and cylinders of varying aspect ratios and/or Reynolds numbers. Reynolds number sweeps provide a sequence of distinct bifurcations which produce significant and measurable differences in the flow field [23]. While there have been studies concentrated on the loading of more complex hub configurations [5,30], there are few studies of the flow topology of the wake behind more complex bodies of revolution. One of these is an investigation by Cannon [25], who experimentally found two counter rotating helical modes in the wake of bullet shaped bodies.

The current objective is the quantification of different sources of hub drag aimed at tightening the tolerances of empirical upper-bound predictions suitable for conceptual design by reference to basic experiments. In addition the current role that computational fluid dynamics (CFD) can realistically contribute to the prediction of drag and wakes to augment experimental studies is examined. These experimental and numerical explorations are designed to advance the state of knowledge for predicting the characteristics and flow phenomena of complex configurations that include flow separation. Recent experimental investigation on a complete helicopter by Gregorio [7] and coupled experimental and CFD investigations by Antoniadis et al. [3] suggest that the main hub wake formation as a reason for the unsteady forces observed on the horizontal stabilizers. Hence, the flow field details could provide useful insights into the well known problem of helicopter “tail shake” [8,12].

2. Methodology

2.1. Experimental methods

Experiments were conducted in the John J. Harper low speed wind tunnel located at the Daniel Guggenheim School of Aerospace Engineering of Georgia Institute of Technology. A generic four-bladed hub model was assembled to approximately one-quarter scale to that of a 10-ton helicopter (Fig. 1).

The model includes structures to represent hub plates, blade shanks, a swashplate, pitch links, drive shaft and the required hardware for assembly. Though greatly simplified from the complexities of full-scale hubs with hydraulic lines and intricate mechanisms, this model provides the interference and flow separation attributed to the full-scale system while maintaining the principal geometric characteristics. The model was adapted into three configurations, as shown in Fig. 2. Configuration 2(a) has unplugged blade shanks, configuration 2(b) has plugged shanks, while configuration 2(c) has plugged shanks and a capped region between the two hub plates.

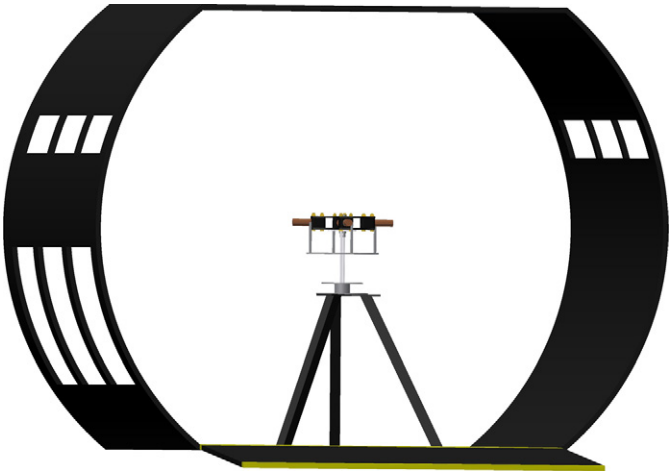

Fig. 1. Hub model setup inside the John J. Harper wind tunnel test section.

The progression of data acquisition and CFD simulation was initiated with static hub tests which were performed on all the configurations to understand the difference in drag behavior. The model was swept through azimuthal orientations for a series of runs performed at zero angle of attack (pitch angle). Six-axis force transducer data were obtained for a 90° azimuthal sweep in 15° increments at a range of tunnel speeds. Subsequently, tests were performed on a rotating hub with the configuration 2(b). A range of rotation rates from 4 to 240 rpm was explored. The test conditions are summarized in Table 1.

In addition, the plugged shank configuration was broken down in stages to measure the individual contribution of each structural component. Since most theoretical drag prediction methods have been developed for the interference effects between two streamlined bodies, or one streamlined body and one less so, for example a wing joint with a fuselage, measuring the interference effects of the hub components was left to experimental trials. Therefore, the hub drag was measured in progression as depicted in the flowchart (Fig. 3). The effect of rotation on the deconstructed model was also measured and is presented in this work.

A detailed velocity map of the hub wake was also obtained via particle image velocimetry. The diagnostics setup for PIV consisted of the laser, camera and sheet optics. The illumination was provided with a Litron double-pulsed Nd:YAG laser (532 nm, 200 mj/pulse) and captured by a LaVision Imager Intense CCD camera (Imager Pro X 2M – 1600 × 1200 pixels, 14 bit). The flow was seeded with 2–3 μm droplets produced with an aerosol seeder. The recording rate is 14 Hz and the time separation between subsequent exposures was set based on the velocity measured in the wind tunnel. One hundred PIV image pairs were acquired for each experiment. The data presented were obtained by averaging the 100 velocity vector fields.

The last experimental technique used in this study was hot-wire anemometry. Experiments were conducted with a single axis hot-wire probe to measure the frequency spectra of velocity fluctuations along the wind tunnel axis. The data were acquired at a sampling frequency of 2000 Hz. Low pass and high pass filters were used to condition the signal before analysis.

2.2. Computational methods

A computational investigation was undertaken using FUN3D [2,4], a NASA developed unstructured solver with overset grid capability. Overset functionality, which is essential to simulate grid

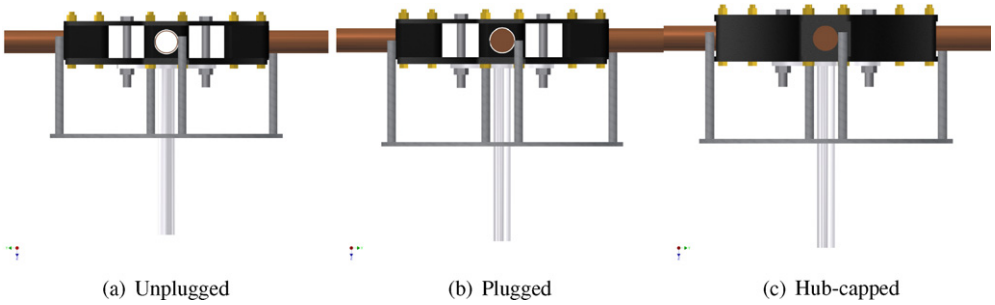

Fig. 2. Three model configurations for static hub experiments and computational simulations.

Fig. 3. Flowchart depicting progression of deconstruction.

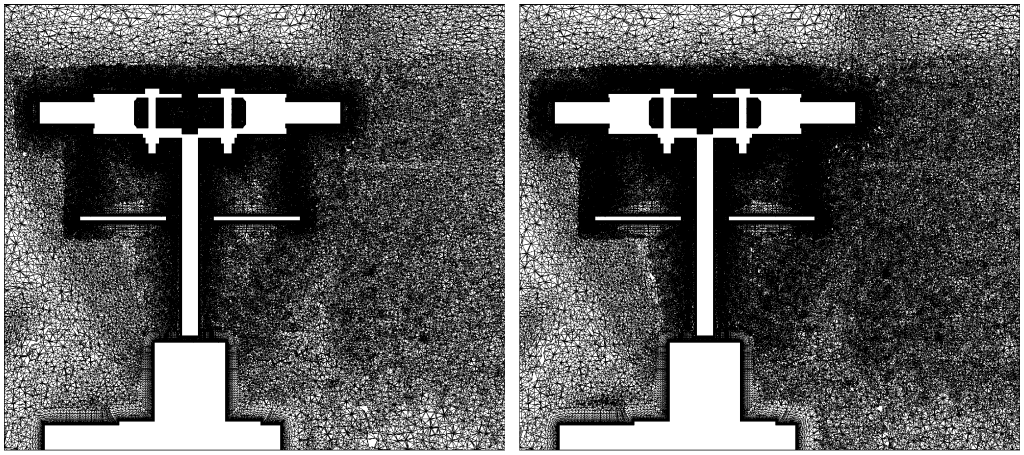

Fig. 4. Refinement of the wake region due to grid adaptation.

Table 1
Summary of experimental test conditions.

Test	Configuration	Azimuth/rpm	Increments	Velocity
Static	2(a), 2(b), 2(c)	0–90°	15°	0–70 mph
Rotating	2(b)	4, 80, 240 rpm	–	0–70 mph

motion of a rotating hub in the presence of a non-rotating test facility or fuselage, is achieved via SUGGAR++ [18] and DiRTlib [17]. FUN3D's capabilities have been successfully applied to rotorcraft applications of both compressible and incompressible regimes [1,15,22]. In order to isolate the effects of the overset grid, both the static and rotating simulations employ overset grids, keeping the same initial near-body grid overlaid on a test facility background grid for both static and rotating simulations.

An overset unstructured grid adaptation capability [19,29] is utilized (Fig. 4) in order to minimize numerical dissipation and computational costs due to prohibitively large grid sizes. The time-dependent adaptation metric used in the present study used the vorticity-magnitude indicator, analogous to the guidelines described by Shenoy et al. [28]. A clear advantage of this technique is that grids may be optimized for different flow conditions and geometric orientations without the need to manually tailor the grid for a particular problem. It is noted that previous numerical investigations [5,30] of hub drag have not examined the ability of grid adaptation to improve predictions of the loading or the flow features of the unsteady wake.

A hybrid Reynolds-averaged Navier–Stokes (RANS) and large eddy simulation (LES) turbulence approach (GT-HRLES) [16] was used to obtain time-accurate evaluations of the unsteady hub wake. This hybrid formulation blends the k–ω SST RANS model with a one-equation LES model for the subgrid-scale turbulence kinetic energy k^{sgs}. The dimensional time step (0.35 ms) was selected equivalent to a 0.5° azimuthal sweep of the 240 rpm rotating hub and is applied to all the cases studied. Each time step was augmented with as many as 40 Newton sub-iterations to increase the temporal accuracy of the simulation. A temporal error controller maintained a specific residual error so that the number of sub-iterations at each time step varied, providing a more efficient scheme without a loss of accuracy. The added computational cost with respect to a RANS-only calculation effectively depends on the number of grid nodes that are required to generate these simulations [16]. On identical grids, the cost of the HRLES model is typically 10–13% greater.

A baseline overset grid of 11.1 million nodes was adapted using vorticity magnitude as the adaptation indicator. Depending on the flow conditions and configuration, the adapted grid sizes varied as described in Table 2. Additional adaptation cycles, as explored by Shenoy and Smith [28] changed the overall performance by less than 1–3%, and thus the grid was deemed sufficient after one adaptation cycle. The background grid included the wind tunnel test section, where walls were modeled as inviscid surfaces. The hub geometry, illustrated in Fig. 5, included the

Table 2
Effect of grid adaptation on the grid size.

Test condition	Initial grid	Adapted
Static hub at 0° orientation ($U_\infty = 30$ mph)	11.1 M nodes	20.9 M nodes
Rotating hub at 240 rpm ($U_\infty = 30$ mph)	11.1 M nodes	29.0 M nodes
Rotating hub at 240 rpm ($U_\infty = 50$ mph)	11.1 M nodes	28.9 M nodes

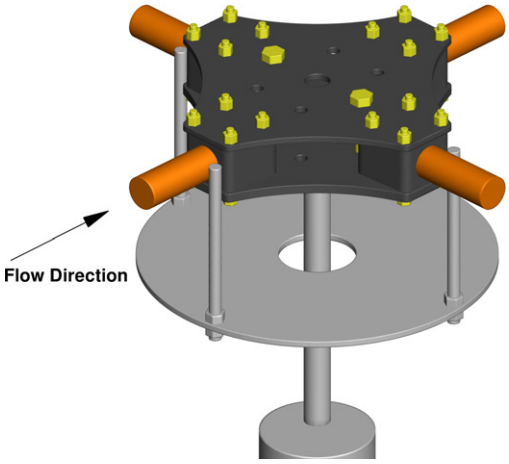

Fig. 5. Hub geometry used for CFD simulations.

details of the model including the pitch links and associated hardware.

3. Results

Results are presented in a progression from integrated loads to flow field details. Both experimental and computational results are used in the following discussions. The results are broken down into three main categories:

1. Static and dynamic force measurements.
2. Wake velocity characterization.
3. Wake frequency spectra.

First, the measurement of integrated drag and side force using experiments and computations at various levels of assembly is discussed. Surface pressure loads presented are from computational results since there is currently no way to measure detailed surface pressure distributions on the components at low dynamic pressures. In addition, the effects of rotation are inferred. Next, the wake velocity field is examined, and CFD correlations are discussed. Finally, the wake frequency spectra are investigated.

3.1. Static and dynamic force measurements

Fig. 6 illustrates the static, rotating and deconstructed hub drag for a range of wind tunnel speeds. Several configurations are shown together to highlight the many qualities of the drag contributions. First, it was observed that the maximum drag is obtained for the static hub when it is oriented at 0° azimuth (blade shanks normal and perpendicular to the free stream). This orientation corresponds to the maximum frontal area of the hub. The 45° static orientation and the hub in rotation at 240 rpm result in nearly the same drag. This result is not unexpected, as the 45° orientation is equivalent to the average frontal area of the hub in rotation. This result is in agreement with previous findings of an investigation performed in the mid-1970's by Sheehy [26] for unfaired hubs.

Excellent agreement between integrated load data and the anisotropically adapted CFD simulation has been found for various test cases. As shown from the linearity of drag with the dynamic pressure in Fig. 7, the data are free of Reynolds number effects for the range of tunnel speeds tested.

The difference in the 0° static orientation and the hub in rotation at 240 rpm was observed in the CFD simulations, where the pressure coefficient distribution over the configuration surface was visualized (Fig. 8). While some features of the pressure distribution are retained, significant pressure decrease (increase in suction peak) was observed on the leading blade shank (left side of figures) and the aft portion of the hub (right side of figures). Interference effects were observed on the left blade shank connector (just below the bolts), where the trailing edge pressure suction shifts to a more forward location from the bottom to top of the connector.

The removal of the blade shanks to examine the deconstructed model indicates that the blade shank contribution to the total drag is negligible. Furthermore, removal of the hub plates reduced the total drag by approximately one-third. Consequently, two-thirds of the hub drag is due to the contributions of the drive shaft, swashplate and pitch link drag. Rotating each of these deconstructed models confirms that there is little variation in drag from the static configuration. The pitch link drag contribution may be computed from the shift in measurements from the prior deconstructed model.

Experimental measurements indicate that the time-averaged force transducer data do not vary with the onset of hub rotation, as noted previously. However, azimuthally varied static hub measurements do capture a variation in the drag with orientation of the model. Note that the measurements shown in Fig. 6(a) do not include the drag due to the motor used in the drive shaft. Static hub load tests were conducted with a hub model which did not allow for high speed rotation. The capped hub configuration creates complete flow blockage through the center of the

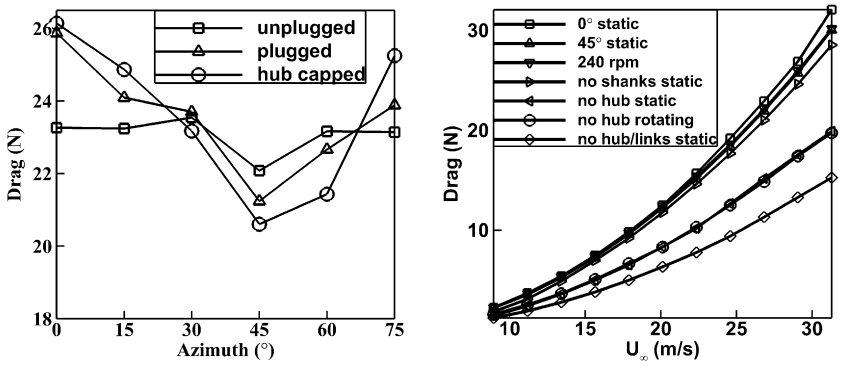

(a) (b)

Fig. 6. Variation of the hub drag with azimuth and free stream velocity.

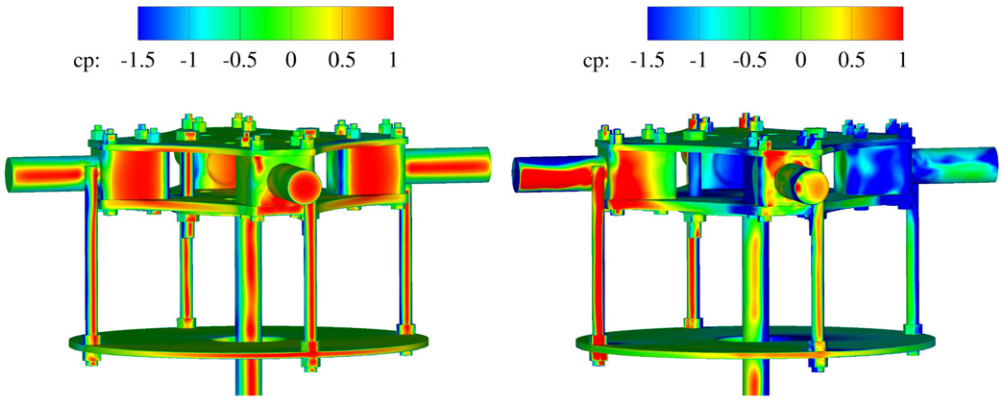

(a) Static hub at 0° orientation (b) Rotating hub at 240rpm

Fig. 8. Comparison of surface pressure distributions obtained from CFD.

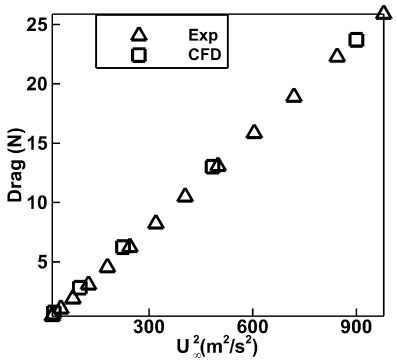

Fig. 7. Correlation between experimental load cell and CFD data for the 0° static hub model.

hub plates and results in the least drag at the 45° static orientation. Therefore, it appears that the drag due to flow separation on the capped configuration is less than the interference drag caused by the channel-like flow through the center of the hub on the non-capped configuration. CFD simulations clearly illustrate this channel-like flow as shown in the center of Fig. 9.

When drag measurements are normalized by the tunnel dynamic pressure, as in Fig. 10, little variation arises over the range of tunnel speeds. The complete model at 0° orientation shows slight Reynolds number effects, however the scaling of the vertical axis may be curtailing the variation.

Collecting load data for a rotating model presents the challenge of decoupling the drag component from the anti-torque of the rotating shaft and motor system. The force transducer is fixed just below a compact high torque stepper motor which drives the hub shaft. Data indicate negligible coupling of the measured torque about the shaft axis and the tunnel axis. This was verified by detailed load cell calibration with the mounted hub model and by comparison of torque measurements with static wind tunnel tests. In order to clarify trends, torque measurements are shown as positive values in Fig. 11(a). However, due to the orientation of the force transducer with respect to the model, measured torques along the drive shaft axis were aligned along the negative z-axis of the load cell.

The torque measured along the drive shaft axis is observed to increase in magnitude with increased rotation rate as delivered by the motor (Fig. 11(a)). The static model also measures an increasing torque for greater tunnel speeds. The model is nearly axially symmetric, however the connection joints of the pitch links to the blade shanks provide some asymmetry, thus generating the measured torque. Further investigation with an axially symmetric model is planned to confirm this assumption.

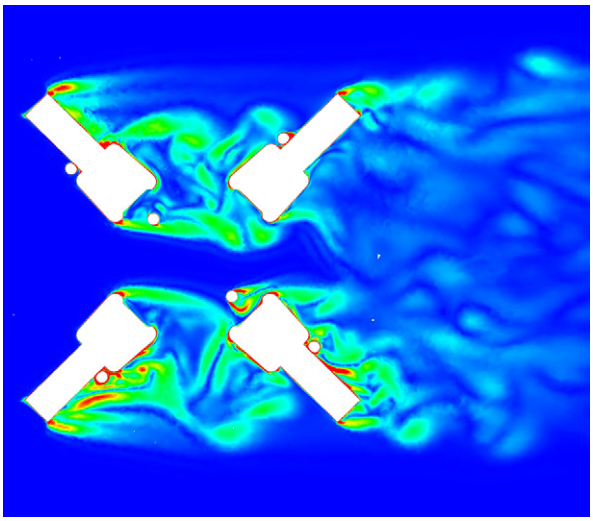

Fig. 9. Vorticity magnitude of the static hub without capped plates at 45° azimuth orientation.

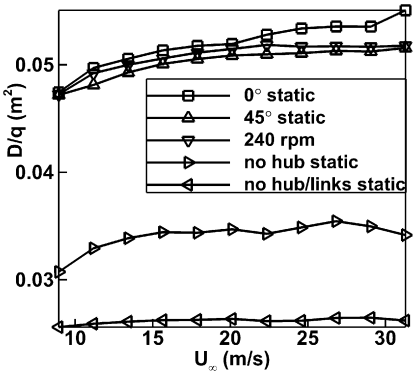

Fig. 10. Drag scaled by tunnel dynamic pressure.

3.1.1. Analysis of side force

Substantial side forces were expected from the rotation of the hub model, based on the classic case of lift generated by a circular cylinder in a normal flow field. However, measurements show little variation in side force due to rotation, and even a reduction of measured side force at greater tunnel speeds (Fig. 11(b)). This feature requires further investigation of scaling effects of the model, and possibly a comparison between the faired case (no flow through the model) and the flow through case. In addition, the dynamic variation of the side force and drag (not shown here) are

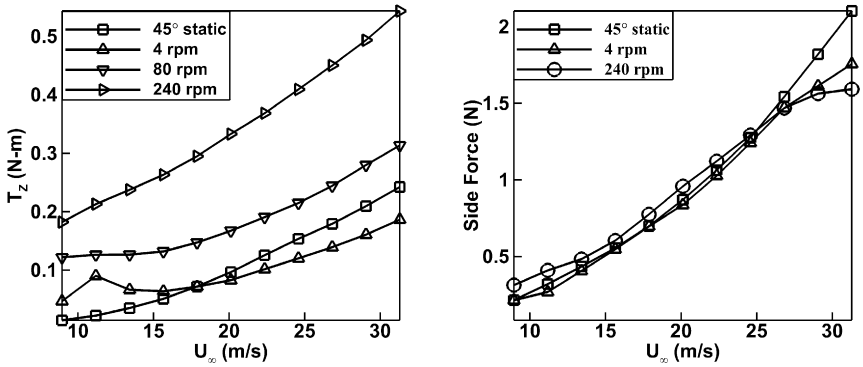

(a) Measured torque along drive shaft axis (b) Side force variation with hub rotation

Fig. 11. Variation in forces with changing rotational and free stream speeds.

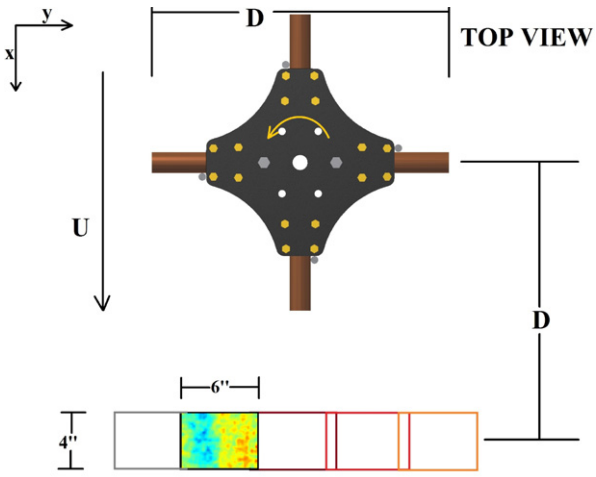

(a) Top view

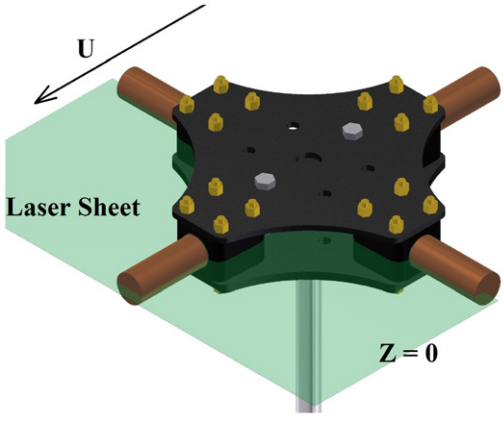

(b) Isometric View

Fig. 12. Map of PIV data collection plane comprised of overlapping stitches.

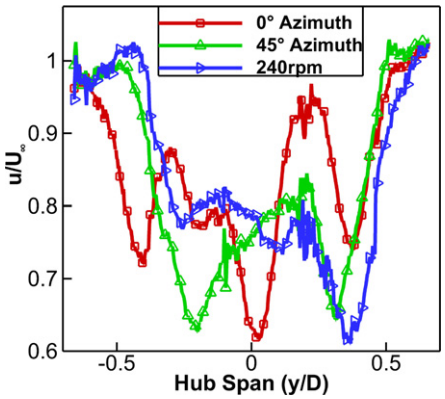

Fig. 13. Wake tunnel axis velocity profiles captured by PIV and scaled by free stream velocity of 20 mph.

substantial, but are mostly due to the periodic components at the 1 and *N* per rev. frequencies. Detailed examination of these aspects, with any dynamic unbalance effects separated out, will be presented in a future publication.

3.2. Wake velocity characterization

The unsteady wake of the hub was characterized through the use of particle image velocimetry (PIV), augmented with CFD. Seeding the flow of a bluff-body wake to the appropriate density for PIV limits the range of tunnel speeds which yield fair resolution. By means of atomized oil as a seeding medium, velocity deficits in the wake at a location one-half of the hub diameter (Fig. 12) have been profiled for several model orientations.

Fig. 13 illustrates the typical variation observed in the wake profile for the hub in two static configurations and one case in rotation. The rotated wake is seen to shift with the hub rotation direction. Also, the free stream region for the rotating case shows an increase in velocity with respect to the tunnel speed setting of 20 mph. The static cases of 0° and 45° show substantial asymmetry, which is interesting as the only asymmetry in the model arises from the pitch link joint with the blade shanks.

CFD predictions were correlated with experimental data (at the PIV measurement location described in Fig. 12) to ascertain the ability of the CFD adapted mesh to capture the details of the wake. Experimental data showed a contraction of the momentum deficit in the hub wake when the model is oriented at 45° azimuth, corresponding to a reduction of hub drag based on frontal area (Fig. 13). The experimental and computational wake velocity deficits correlated very well, as illustrated by Fig. 14. These results provide implications for momentum integral drag resolution via flow computation when overset grid adaptation is applied. The causal wake behavior that drives the momentum deficits observed in Fig. 14 is clearly illustrated by the CFD velocity contours downstream of the hub (Fig. 15). The largest deficit at the static hub centerline is clearly defined by the strong velocity deficit just behind the hub main shaft. The two secondary wake deficits appear behind the pitch links to the left and right of the hub shaft. When the hub rotates in a counter clockwise direction, the primary velocity deficit is translated upward and to the right, appearing behind the right (aft looking forward) blade shank. The velocity deficit due to the main drive shaft appears to have coalesced with that of the right pitch link. There remains only a weaker, secondary velocity deficit

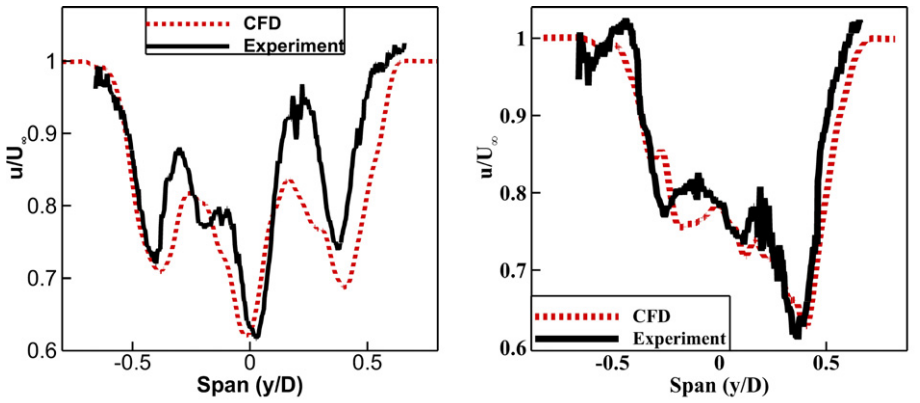

(a) Static hub at 0° orientation (b) Counter clockwise rotating hub at 240 rpm

Fig. 14. Comparison of PIV and CFD data for the tunnel axis wake velocity deficit.

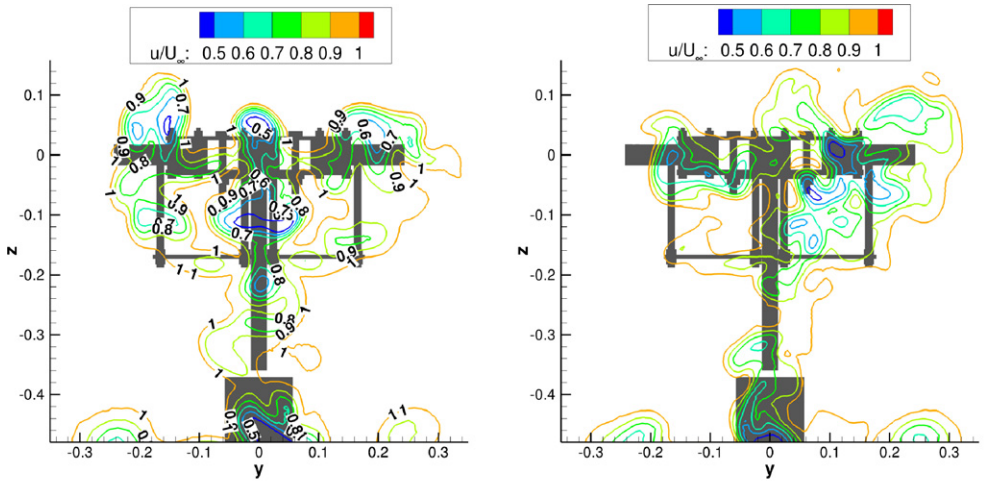

(a) Static hub at 0° azimuth orientation (b) Counter clockwise rotating hub at 240 rpm

Fig. 15. CFD velocity contours at $x = 1$D downstream of the hub center.

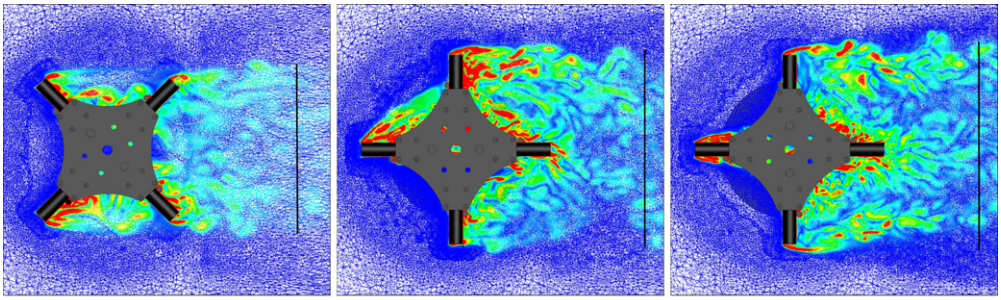

(a) Static at 45° orientation (b) Rotating (c) 0° Static orientation

Fig. 16. Illustration of the wake extent (via vorticity contours).

from the left pitch link, which has also translated in the positive y-direction (to the right) of the flow induced by the counter clockwise rotation.

Further insights into the character of the flow at and behind the hub were obtained from the CFD simulations. Consider for example, the velocity contours presented in planform view (looking down on the rotor hub) in Fig. 16 for the static 45° azimuth, rotating, and static 0° azimuth cases (the solid black line on the right of each figure indicates the downstream location of the velocity contours presented in Fig. 15). As noted previously in the discussion of the force measurements, the drag for the rotating hub is similar to the drag of the static 45° azimuth orientation. The effects of rotation yield a contracted wake span similar to the 45° static case when compared to the 0° orientation (Fig. 15(b)). The rotation causes significant vortex shedding from the blade shanks, similar to the bluff-body shed wake of the shanks when they are obliquely aligned with the free stream.

The importance of overset adaptation is illustrated in Figs. 17 and 18. A summary of the grid size growth due to adaptation is given in Table 2. The initial grid, generated using VGRID [20], provided *a priori* refinement of the grid in the near body; however, it clearly does not capture the extent and magnitude of the near-body vorticity shed from the main drive shaft, pitch links and blade shanks. The wake in the region between 1/2 to 1 hub diam-

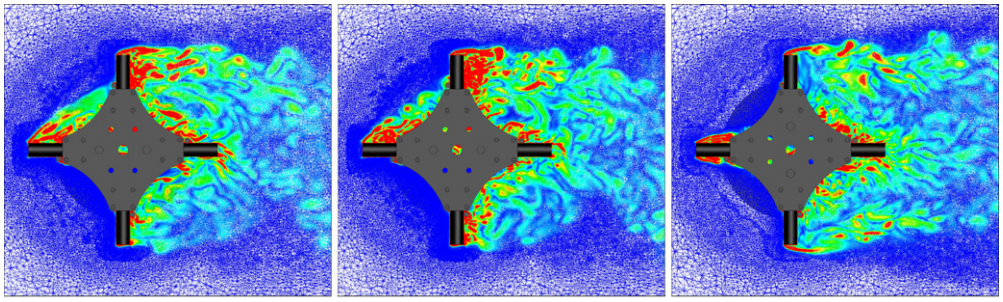

(a) Initial rotating grid (b) Adapted rotating grid (c) Adapted 0° azimuth static grid

Fig. 17. Planform (looking down) view of the vorticity magnitude for the initial and adapted grid.

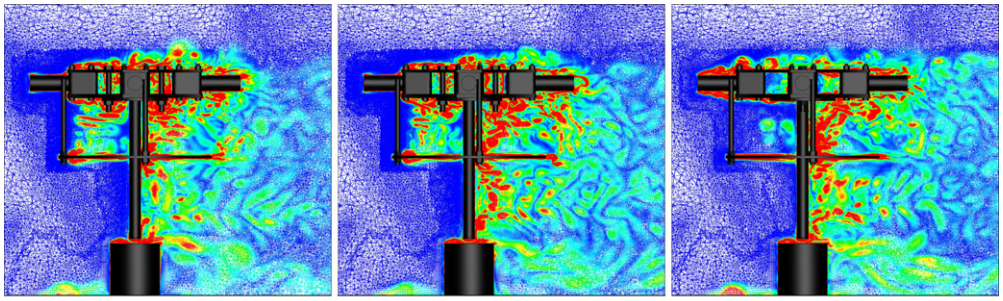

(a) Initial rotating grid (b) Adapted rotating grid (c) Adapted 0° azimuth static grid

Fig. 18. Left (looking forward) side view of the vorticity magnitude for the initial and adapted grid.

eter downstream also shows increased vorticity content when the grid is adapted. In particular for Fig. 18, the results on the initial grid imply significantly more interference effects on the main drive shaft and pitch links than is observed with the adapted grid, which could suggest erroneous conclusions during drag deconstruction.

3.3. Wake frequency spectra

A single axis hot-film constant temperature anemometer sensor measured velocity fluctuations in the hub wake. Samples were collected at four locations on a plane bisecting the hub for the static hub oriented at 0° as in Fig. 19. Data were also collected at the same locations for the rotating hub (240 rpm). Power spectral density (PSD) plots from both experiment and CFD for the static and rotating tests at a 30 mph free stream speed are presented in Figs. 20 and 21. The spectra were obtained by applying a correction for hot-wire sensitivity suggested by Champagne and Sleicher [6].

Both experimental sets of PSD show an increase in broadband turbulence as the sensor is placed further inboard. The power spectra plots generally compare well against the 5/3 law, characterizing homogeneity of turbulence [21]. A study of the shedding frequencies of bluff bodies by Sakamoto and Arie [24] provides Strouhal numbers of circular cylinders of varying aspect ratios. Their predicted shedding frequencies are in agreement with the blade shank frequency of approximately 50 Hz, observed in locations 2 and 3 of the static test (Fig. 20), just behind the shank. There is a noticeable amplitude spike for all sampling locations of the rotating test case that corresponds to the predicted 4 per revolution signal of the 4-bladed hub model. Both the experimental and CFD efforts capture this 16 Hz frequency as the hub rotates at 240 rpm (4 rev./s). The next harmonic of this frequency (8 per rev.) is greatly amplified at the inboard sampling location, well within the wake region.

Better agreement with 5/3 law slope is observed for both the experimental and CFD results at inboard locations. The turbulence displays an expected broad range of scales in the bluff-body wake region. To examine the character of the CFD simulation, contours

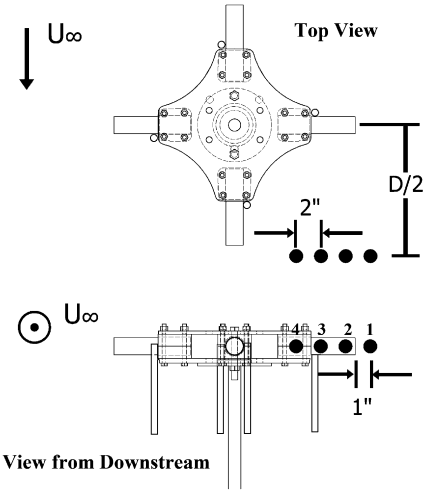

Fig. 19. Downstream hot-wire measurement locations.

of the HRLES turbulence model's blending function are given in Fig. 22. Values near 1 indicate that the RANS formulation is in effect and values near 0 indicate regions dominated by LES. The four locations show that the flow field in this region of the wake displays LES behavior, enabling the simulation to capture of the broad range of turbulent scales obtained in the power spectra. Confidence was established in the selection of the time step by obtaining converged spectra between the current time step $\Delta t = 0.3472$ ms and a coarser time step $\Delta t = 0.6944$ ms, plotted in Fig. 23.

In addition to the 30 mph free stream results, tests were conducted at 50 mph for the rotating case at 240 rpm. The resulting power spectrum is plotted in Fig. 24. The spectral features are in general agreement with those of the 30 mph free stream case. These include the 4 per rev. and 8 per rev. peaks and the increasing power magnitude and range of turbulent scales at the inboard locations.

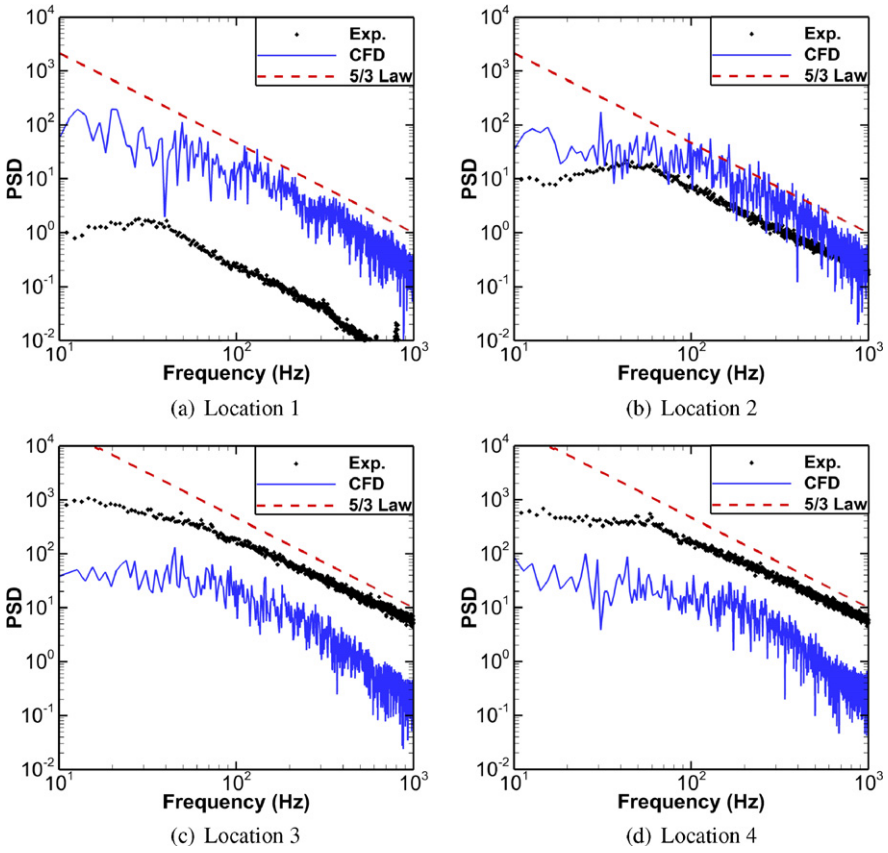

Fig. 20. PSD of velocity fluctuations in the hub wake for the static hub at 0° orientation at 30 mph.

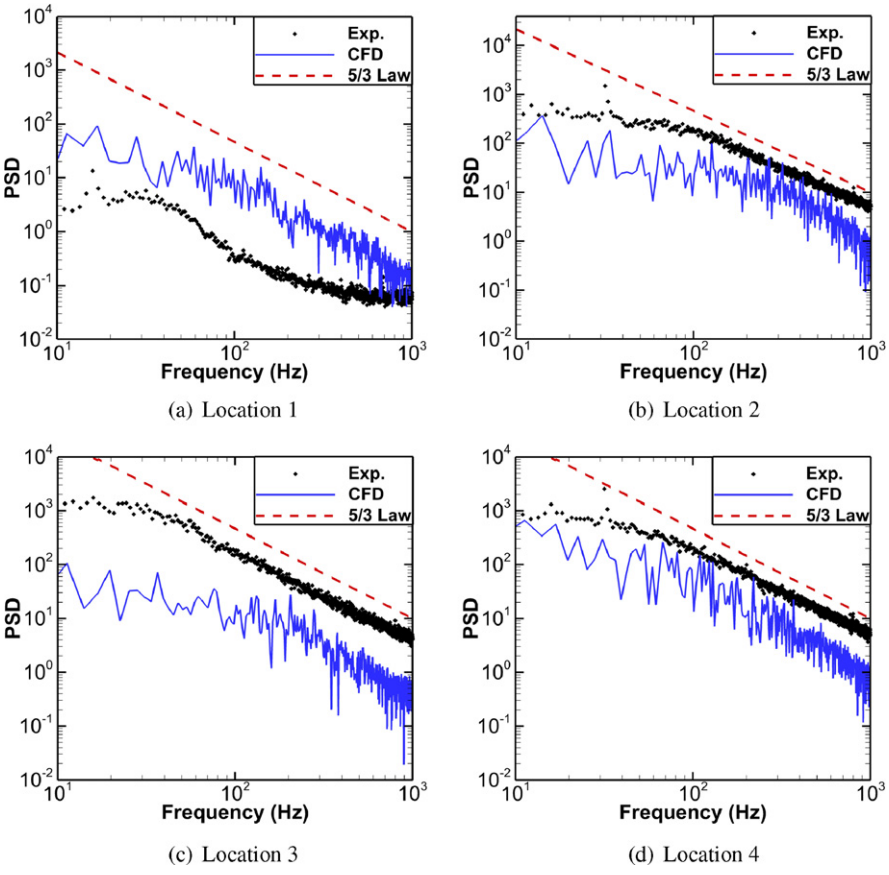

Fig. 21. PSD of velocity fluctuations in the hub wake for the rotating hub at 240 rpm at 30 mph.

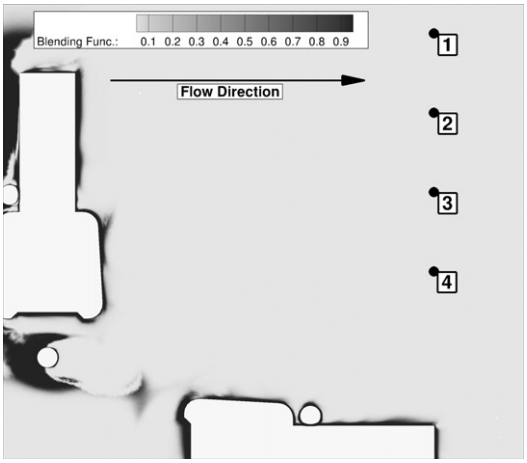

Fig. 22. Top view of HRLES blending function contours.

The PSD plots (Figs. 20, 21 and 24) show some disagreement in the magnitude of power obtained between experiment and CFD. The general observation is an over-prediction in power obtained by CFD at location 1. Examination of the wake features in this region (Fig. 25) indicates that the CFD shear layer prediction coincides with location 1, indicating a larger extent of the wake region than that observed in the experiment. This is further substantiated by the wake velocity profiles in Fig. 14, where the extent of the CFD wake is greater in the positive y side – the region where power spectra are compared. Location 1 corresponds to the spanwise distance $y/D = 0.55$, where the velocity magnitude of both the static (Fig. 14(a)) and rotating cases appears shifted. In the static test case (Fig. 14(a)), the profile shift is noted for a significant portion of the wake. However, the improved velocity correlation for the rotating test case (Fig. 14(b)) at the inboard locations concurs with the turbulence levels that show more accurate agreement. Further, there may be local spatial shifts in features detected indicating that the adaptation methodology may need to be locally enhanced in order to propagate wake features more accurately. Additional experiments may be warranted to test the accuracy of these improvements.

4. Conclusions

Experimental and computational efforts have been utilized to obtain the character of the integrated loads and complex wake flow field of a scaled helicopter main rotor hub. The current investigation has yielded these conclusions:

1. Large regions of separated flow contribute to considerable drag from the complex hub. The azimuthal variation of the static hub model shows variation in drag corresponding to the projected frontal area of the hub. For the four-bladed hub configuration, the 45° azimuthal orientation yields nearly identical drag measurements to the mean values obtained for the rotating hub.
2. Side force and torque are present for the static model due to small axial asymmetries in the assembly such as pitch links offset from the shank axes. For both static and rotating cases, the side force is approximately 1/15 the magnitude of the drag. The use of a 6-axis force transducer has shown sufficient accuracy and the ability to capture the anti-torque contribution of the rotating hub shaft while providing decoupled drag and side force measurements.
3. Initial deconstruction of the hub configuration has provided insight into the drag breakdown and interference effects of geometric components. At the Reynolds numbers and free stream velocities examined, the hub plates and blade shanks contribute approximately 1/3 of the hub drag, while the

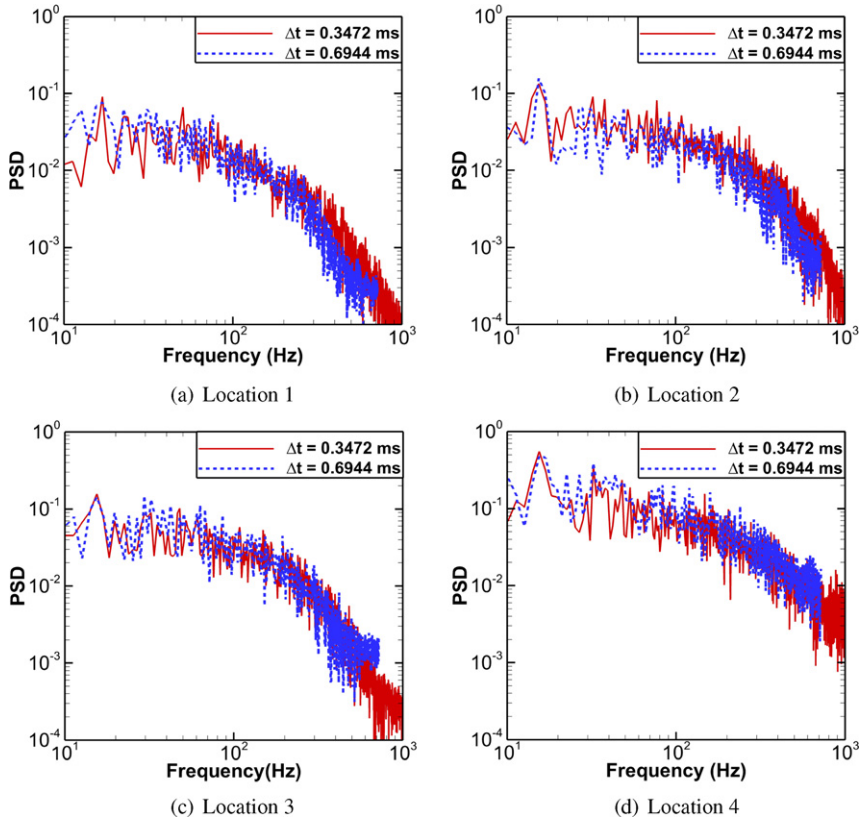

Fig. 23. Normalized PSD of velocity fluctuations in the hub wake for the rotating hub at 240 rpm at 30 mph.

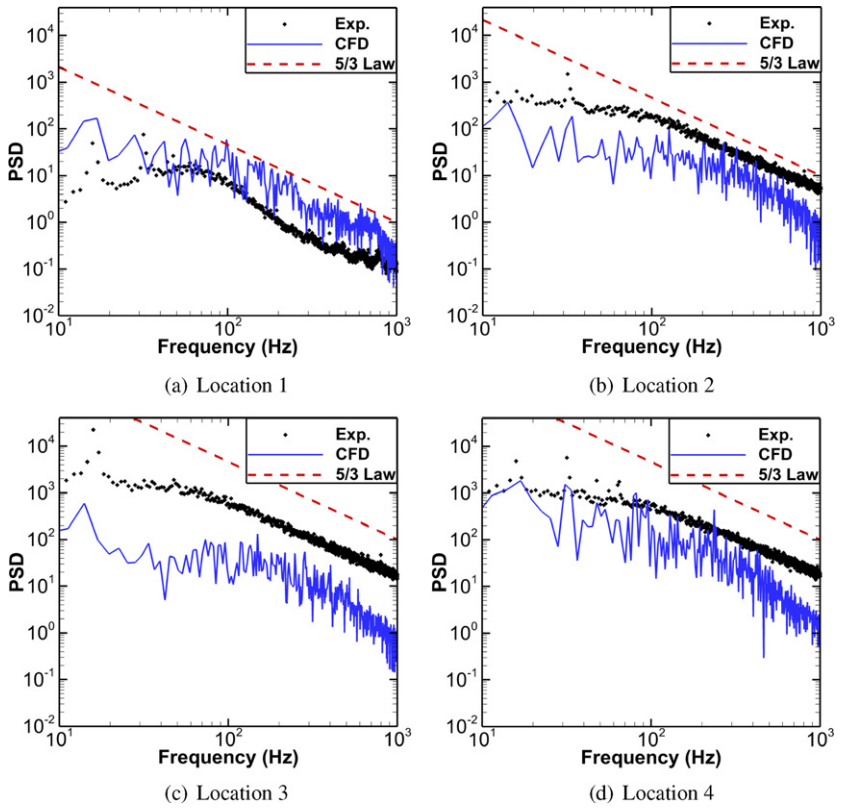

Fig. 24. Power density spectrum of velocity fluctuations in the hub wake for the rotating hub at 240 rpm at 50 mph.

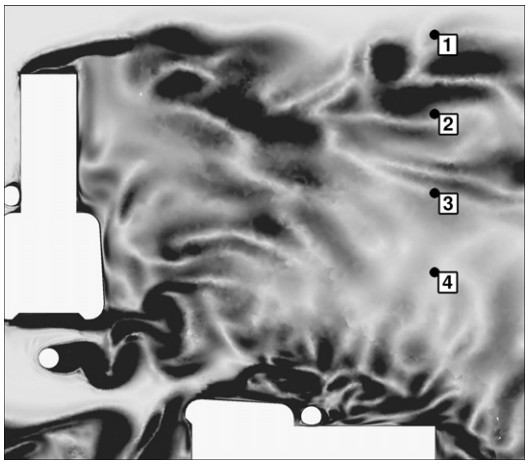

Fig. 25. Top view of vorticity contours for the static hub ($U_\infty = 30$ mph).

remaining contribution is due to flow separation about the drive shaft, pitch links and swashplate in that order. Rotation effects on the deconstructed model are observed to be minimal at the flow conditions evaluated.

4. The resolution of PIV in the hub wake has proven sufficient to detect sideward shifts in the wake velocity deficit due to hub rotation. Variations in the static hub model orientation have also been captured by PIV in the wake field, with asymmetry attributed to the pitch link to blade shank interaction. This is reinforced by the pressure coefficient distribution of the pitch link and blade shanks simulated via CFD. The resolution of drag from components appears to be feasible using wake velocity field results, which is reinforced via excellent correlation between the experimental and CFD results.
5. Computational prediction at the fidelity level of the FUN3D Navier–Stokes solver, has been shown to be an invaluable tool to augment experimental analyses for this complex hub configuration. Strong correlations between CFD and both experiment load and PIV data permit the utilization of the surface and flow field characteristics predicted by CFD to further explain and clarify the causal physics due to the complex hub geometry.
6. New CFD capabilities developed to permit unstructured overset anisotropic feature-based adaptation across both background and near-body grids are essential to capture the correct physics of complex configurations where significant wake interactions occur in both the near- and far-field grids.
7. The application of the newly developed feature-based overset grid adaptation is beneficial not only for the accurate prediction of the time-averaged wake velocity profiles but also in order to capture the turbulent content of the flow. The methodology complements the HRLES turbulence model which enables a physics-based model of small scale features.

Acknowledgements

The authors gratefully acknowledge the support of the Office of Naval Research and the associated technical monitor, Dr. Judah Milgram. Assistance from Felipe Ortega, Alex Forbes, Ryan McGowan and Rafael Lozano for the experimental data acquisition and reduction and from Marlin Holmes for the CFD data reduction is acknowledged and greatly appreciated by the authors.

References

[1] J.N. Abras, Enhancement of aeroelastic rotor airload prediction methods, Ph.D. thesis, Georgia Institute of Technology, 2009.
[2] W.K. Anderson, R.D. Rausch, D.L. Bonhaus, Implicit/multigrid algorithms for incompressible turbulent flows on unstructured grids, Journal of Computational Physics 128 (2) (1996) 391–408.

[3] A. Antoniadis, D. Drikakis, B. Zhong, G. Barakos, R. Steijl, M. Biava, L. Vigevano, A. Brocklehurst, O. Boelens, M. Dietz, Assessment of CFD methods against experimental flow measurements for helicopter flows, Aerospace Science and Technology 19 (1) (2012) 86–100.
[4] D.L. Bonhaus, An upwind multigrid method for solving viscous flows on unstructured triangular meshes, Ph.D. thesis, University of Cincinnati, 1993.
[5] J.O. Bridgeman, G.T. Lancaster, Physics-based analysis methodology for hub drag prediction, in: Proceedings of the 66th Annual Forum of the American Helicopter Society, Phoenix, AZ, 2010.
[6] F. Champagne, C. Sleicher, Turbulence measurements with inclined hot-wires. Part 2. Hot-wire response equations, Journal of Fluid Mechanics 28 (1) (1967) 177–182.
[7] F. De Gregorio, Flow field characterization and interactional aerodynamics analysis of a complete helicopter, Aerospace Science and Technology 19 (1) (2012) 19–36.
[8] P. de Waard, M. Trouve, Tail shake vibration in flight – objective comparison of aerodynamic configurations in a subjective environment, in: Proceedings of the 55th Annual Forum of the American Helicopter Society, Montreal, Canada, 1999, pp. 2306–2316.
[9] R.E. Gormont, Some important practical design constraints affecting drag reduction, in: Proceedings of the 31st Annual Forum of the American Helicopter Society, Washington, DC, 1975.
[10] J.W. Gregory, C.O. Porter, T.E. McLaughlin, Circular cylinder wake control using spatially distributed plasma forcing, in: 4th AIAA Flow Control Conference, Seattle, WA, 2008.
[11] J. Hoffman, The relationship between rotorcraft drag and stability and control, in: Proceedings of the 31st Annual Forum of the American Helicopter Society, Washington, DC, 1975.
[12] I.S. Ishak, S. Mansor, T. Mat Lazim, Experimental research on helicopter tail shake phenomenon, in: Proceedings of the 2nd Regional Conference on Vehicle Engineering & Technology, Hotel Istana, Kuala Lumpur, 2008.
[13] A. Kerr, Effect of helicopter drag reduction on rotor dynamic loads and blade life, in: Proceedings of the American Helicopter Society Symposium on Helicopter Aerodynamic Efficiency, Washington, DC, 1975.
[14] C.N. Keys, R. Wiesner, Guidelines for reducing helicopter parasite drag, Journal of the American Helicopter Society 20 (1) (1975) 31–40.
[15] C.E. Lynch, Advanced CFD methods for wind turbine analysis, Ph.D. thesis, Georgia Institute of Technology, 2011.
[16] C.E. Lynch, M.J. Smith, Extension and exploration of a hybrid turbulence model on unstructured grids, AIAA Journal 49 (11) (2011) 2585–2590, http://dx.doi.org/10.2514/1.56296.
[17] R. Noack, DiRTlib: A library to add an overset capability to your flow solver, in: Proceedings of the 17th AIAA Computational Fluid Dynamics Conference, 2005.
[18] R. Noack, D. Boger, R. Kunz, P. Carrica, SUGGAR++: An improved general overset grid assembly capability, in: Proceedings of the 19th AIAA Computational Fluid Dynamics Conference, 2009.
[19] F. Ortega, R. Shenoy, V. Raghav, M. Smith, N. Komerath, Deconstructing hub drag, in: Proceedings of the 29th AIAA Applied Aerodynamics Conference, Honolulu, HI, 2011, AIAA-2011-3821.
[20] S. Pirzadeh, Unstructured viscous grid generation by the advancing-layers method, AIAA Journal 32 (8) (1994) 1735–1737.
[21] S.B. Pope, Turbulent Flows, Cambridge Univ. Press, New York, NY, 2000.
[22] T. Renaud, D. O'Brien, M. Smith, M. Potsdam, Evaluation of isolated fuselage and rotor–fuselage interaction using computational fluid dynamics, Journal of the American Helicopter Society 53 (1) (2008) 3–17.
[23] A. Roshko, Perspectives on bluff body aerodynamics, Journal of Wind Engineering and Industrial Aerodynamics 49 (1) (1993) 79–100.
[24] H. Sakamoto, M. Arie, Vortex shedding from a rectangular prism and a circular cylinder placed vertically in a turbulent boundary layer, Journal of Fluid Mechanics 126 (1) (1983) 147–165.
[25] J. Seidel, S. Siegel, K. Cohen, T. McLaughlin, Simulations of flow control of the wake behind an axisymmetric bluff body, in: 3rd AIAA Flow Control Conference, San Francisco, CA, 2006, AIAA-2006-3490.
[26] T.W. Sheehy, A general review of helicopter rotor hub drag data, Journal of the American Helicopter Society 22 (2) (1977) 2–10.
[27] T.W. Sheehy, D.R. Clark, A method for predicting helicopter hub drag, Tech. Rep., United Technologies Corporation, Sikorsky Aircraft Division, Stratford, CT, 1976.
[28] R. Shenoy, M. Holmes, M.J. Smith, N.M. Komerath, Computational investigation of hub drag deconstruction from model to full scale, in: Proceedings of the 37th European Rotorcraft Forum, Milan, Italy, 2011. See also R. Shenoy, M. Holmes, M.J. Smith, N. Komerath, Scaling evaluations on the drag of hub system, Journal of the American Helicopter Society.
[29] R. Shenoy, M. Smith, Unstructured overset adaptive mesh refinement for rotorcraft aerodynamic interactions, in: Proceedings of the 67th Annual Forum of the American Helicopter Society, Virginia Beach, VA, 2011.
[30] B. Wake, E. Hagen, S. Ochs, C. Matalanis, Assessment of helicopter hub drag prediction with an unstructured flow solver, in: Proceedings of the 65th Annual Forum of the American Helicopter Society, Fort Worth, TX, 2009.
[31] R.M. Williams, P.S. Montana, A comprehensive plan for helicopter drag reduction, Tech. Rep. 19750054284, NASA, 1975.